Bioconjugate Chemistry

Article

pubs.acs.org/bc

Synthesis, Characterization, and Application of Core−Shell $Co_{0.16}Fe_{2.84}O_4$@$NaYF_4$(Yb, Er) and Fe_3O_4@$NaYF_4$(Yb, Tm) Nanoparticle as Trimodal (MRI, PET/SPECT, and Optical) Imaging Agents

Xianjin Cui,[†] Domokos Mathe,[‡] Noémi Kovács,[‡] Ildikó Horváth,[§] Maite Jauregui-Osoro,[†] Rafael Torres Martin de Rosales,[†,∥] Gregory E. D. Mullen,[†] Wilson Wong,[⊥] Yong Yan,[#] Dirk Krüger,[†] Andrei N. Khlobystov,[#] Maria Gimenez-Lopez,[#] Mariann Semjeni,[‡] Krisztián Szigeti,[§] Dániel S Veres,[§] Haizhou Lu,[¶] Ignacio Hernández,[□] William P. Gillin,[¶] Andrea Protti,[†] Katalin Kis Petik,[§] Mark A. Green,[*,†,∥,▲] and Philip J. Blower[*,†,∥]

[†]King's College London, Division of Imaging Sciences and Biomedical Engineering, Fourth Floor Lambeth Wing, St. Thomas Hospital, London, SE1 7EH, United Kingdom

[‡]CROmed Ltd. Baross u. 91-95, H-1047, Budapest, Hungary

[§]Department of Biophysics and Radiation Biology, Semmelweis University, IX. Tűzoltó u. 37-47, H-1094, Budapest, Hungary

[∥]King's College London, Division of Chemistry, Britannia House, 7 Trinity St., London, SE1 1DB, United Kingdom

[⊥]MRC Centre for Transplantation, King's College London, Guys Hospital, London, SE1 9RT, United Kingdom

[#]School of Chemistry, Nottingham University, Nottingham, NG7 2RD, U.K.

[¶]School of Physics and Astronomy, Queen Mary University of London, Mile End Road, London, E1 4NS, United Kingdom

[□]Dpto. CITIMAC, Universidad de Cantabria, Avda. Los Castros, s/n 39005, Santander, Spain

[▲]King's College London, Department of Physics, Strand Campus, London, WC2R 2LS, United Kingdom

Supporting Information

ABSTRACT: Multimodal nanoparticulate materials are described, offering magnetic, radionuclide, and fluorescent imaging capabilities to exploit the complementary advantages of magnetic resonance imaging (MRI), positron emission tomography/single-photon emission commuted tomography (PET/SPECT), and optical imaging. They comprise Fe_3O_4@$NaYF_4$ core/shell nanoparticles (NPs) with different cation dopants in the shell or core, including $Co_{0.16}Fe_{2.84}O_4$@$NaYF_4$(Yb, Er) and Fe_3O_4@$NaYF_4$(Yb, Tm). These NPs are stabilized by bisphosphonate polyethylene glycol conjugates (BP-PEG), and then show a high transverse relaxivity (r_2) up to 326 mM^{-1} s^{-1} at 3T, a high affinity to [^{18}F]-fluoride or radiometal-bisphosphonate conjugates (e.g., ^{64}Cu and ^{99m}Tc), and fluorescent emissions from 500 to 800 nm under excitation at 980 nm. The biodistribution of intravenously administered particles determined by PET/MR imaging suggests that negatively charged $Co_{0.16}Fe_{2.84}O_4$@$NaYF_4$(Yb, Er)-BP-PEG (10K) NPs cleared from the blood pool more slowly than positively charged NPs Fe_3O_4@$NaYF_4$(Yb, Tm)-BP-PEG (2K). Preliminary results in sentinel lymph node imaging in mice indicate the advantages of multimodal imaging.

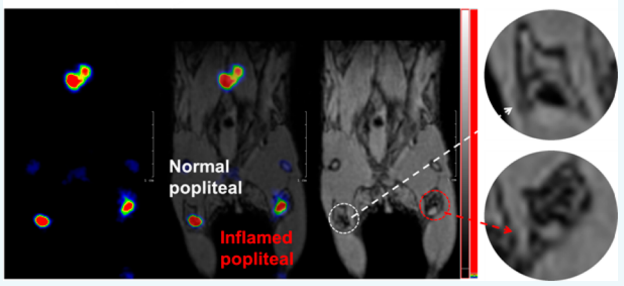

INTRODUCTION

The potential clinical and biomedical application of synergistic combinations of magnetic resonance imaging (MRI) with other biomedical imaging modalities, especially positron emission tomography (PET) and optical imaging, has become an emerging topic in the last ten years.[1−3] Combinations of imaging modalities have the potential to overcome the respective limitations of the individual imaging techniques and provide more accurate and complete physiological and anatomical information for diagnosis and therapy.[4−7] In certain applications, the combination of imaging techniques into a single contrast agent could also offer the benefits of a reduced dose of contrast agent, a shorter procedure time for both patients and scanners, and the assurance that the different scans reflect contrast located in the same physiological conditions and spatial position.[8,9] Compared with small molecules or bioconjugates widely used in research and the clinic, nano-

Special Issue: Molecular Imaging Probe Chemistry

Received: June 16, 2015
Revised: July 14, 2015
Published: July 14, 2015

DOI: 10.1021/acs.bioconjchem.5b00338
Bioconjugate Chem. 2016, 27, 319−328

particles (NPs) allow an enhanced imaging signal due to their high payload, as well as a high avidity via multiple targeting ligands attached to their surface.[10] In addition, T_2 or T_2* contrast in MRI inherently requires that the contrast agents are particulate. As fluorescent probes, inorganic NPs can not only provide more intense and stable emissions (with peaks tunable from the visible to the near-infrared region), but are generally more thermally stable under laser illumination than organic molecular dyes.[9,11] The majority of current multimodality contrast agents are based on superparamagnetic iron oxide NPs,[12−14] while a few examples of Gd[15,16] or Mn[17] containing NPs have also been reported. Since Weissleder et al.[18] reported their pioneering work on multimodal imaging, combinations of NPs and functional polymers[19] or polydentate ligands[8,20,21] have been widely applied to obtain multifunctional agents.[14,15] An alternative approach is hybrid inorganic nanocomposites containing two materials with different properties, such as Fe_3O_4@$NaGdF_4$ NPs,[22] $NaYF_4$@Fe_xO_y,[23] and Fe_3O_4@LnF_3.[24] For these hybrid inorganic NPs to be used as multimodal imaging contrast, however, a well-defined core−shell structure is crucial to avoid the possibility that some fractions of the NPs behave differently from other fractions, and as a result different imaging modalities reflect the contrast located in different spatial positions.

In this report, we set out to design a trimodal system comprising a magnetic and a fluorescent component with rapid, facile, and efficient radiolabeling under sterile, GMP (Good Manufacturing Practice) conditions with minimal manipulation. Ideally, the system must have a well-defined structure to ensure that the properties do not vary between particles and that the signals of different modalities do not come from the different particle types with potentially different in vivo locations. On the basis of this principle, superparamagnetic iron oxide (and its analogues) and $NaYF_4$ were selected as the core and shell, respectively, of the proposed combined system. As a well-known host material for up-conversion fluorescence, $NaYF_4$ was also reported to be efficient as a substrate for [^{18}F]-fluoride labeling although the detailed mechanism remains unclear.[15,25−31] Such a system would allow us to tune the fluorescent properties by doping the $NaYF_4$ shell with different lanthanide cations, and optimize magnetic properties by altering the core−shell ratio or the size and composition of the magnetic core. The bisphosphonate affinity[32] of the $NaYF_4$ shell also affords the capability for surface derivatization with radionuclides and with targeting molecules or polymers to control solubility and in vivo behavior.

RESULTS

Structure, Morphology, Composition, and Colloidal Stability of NPs. Fe_3O_4@$NaYF_4$ core/shell NPs were synthesized by a two-step thermolysis approach using iron pentacarbonyl and trifluoroacetate salts (Scheme S1 in Supporting Information). Lanthanide cations (Yb, Er, or Tm) were doped into the $NaYF_4$ shell for the purpose of up-conversion fluorescence, and Co was doped into the Fe_3O_4 core to adjust the magnetic property of NPs. Transmission electron microscope (TEM) images (Figure 1) revealed that the NPs with different doping shared a similar size and morphology. X-ray powder diffraction (XRD) patterns implied that these Fe_3O_4@$NaYF_4$ core/shell NPs consisted of two distinct phases, Fe_3O_4 and α-$NaYF_4$ (Figure S1). High resolution transmission electron micrograph (HRTEM) studies of NPs Fe_3O_4@$NaYF_4$(Yb, Tm) showed atomic lattice fringes of 2.97 Å

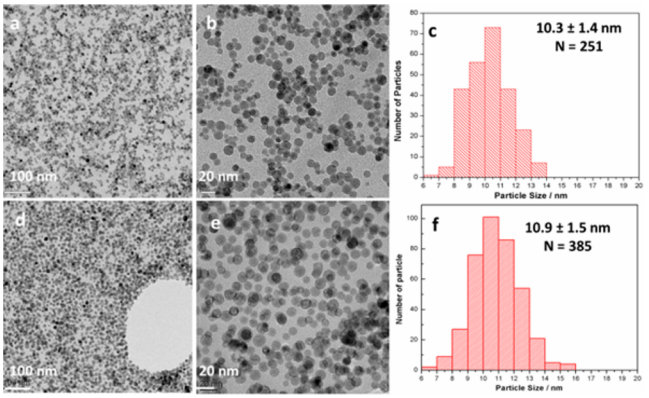

Figure 1. TEM images at low and high magnifications, and the size distribution of $Co_{0.16}Fe_{2.84}O_4$@$NaYF_4$(Yb, Er) NPs (a−c) and Fe_3O_4@$NaYF_4$(Yb, Tm) NPs (d−f). The particle size was determined on TEM and N is the number of particles counted for size analysis.

associated with the (022) and (202) planes of cubic Fe_3O_4 and 1.72 and 2.94 Å corresponding to the (022) and (200) planes of cubic $NaYF_4$, respectively (Figure 2a). The angle between the (022) and (202) planes was calculated as 60°, consistent with the value measured on the HRTEM image. The electron diffraction patterns were obtained by the fast Fourier transform analysis of the HRTEM image. Two sets of diffraction patterns for Fe_3O_4 and $NaYF_4$ were obtained, and each spot was

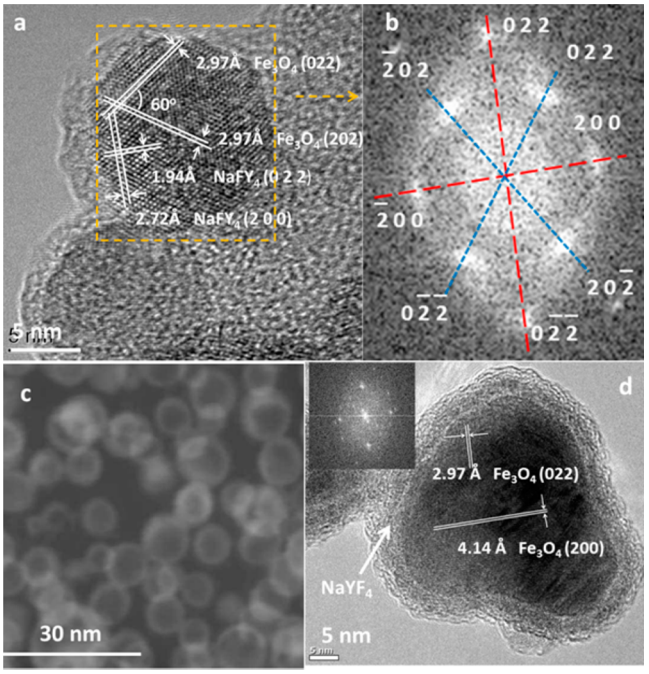

Figure 2. HRTEM studies of NPs: (a) HRTEM images of Fe_3O_4@$NaYF_4$(Yb, Tm); (b) fast Fourier transform of the selected area in part a, showing two sets of diffraction patterns. The diffraction pattern marked in blue belonged to cubic Fe_3O_4, and the one marked in red was assigned as cubic $NaYF_4$; (c) high angle annular dark field image of Fe_3O_4@$NaYF_4$(Yb, Tm), showing the Z contrast difference between the shell and core of particles induced by a slightly higher average atomic number in the shell after doping with heavy atoms Yb and Tm; (d) HRTEM image revealed the core−shell structure of NP $Co_{0.16}Fe_{2.84}O_4$@$NaYF_4$(Yb, Er). Atomic lattice fringes 2.97 and 4.14 Å corresponded to (022) and (200) planes of Fe_3O_4, respectively. The inset is a fast Fourier transform of the micrograph.

DOI: 10.1021/acs.bioconjchem.5b00338
Bioconjugate Chem. 2016, 27, 319−328

assigned as indicated in Figure 2b. Analysis of the electron diffraction patterns indicated that core−shell structures were formed by growing the $(01\bar{1})$ plane of $NaYF_4$ on the $(11\bar{1})$ plane of Fe_3O_4 with a rotation angle of 30°. High angle annular dark field (HAADF, or *Z* contrast) imaging was employed to investigate the structure of NP Fe_3O_4@$NaYF_4$(Yb, Tm), as its contrast was strongly dependent on average atomic number of the specimen but insensitive to its thickness. The HAADF image of Fe_3O_4@$NaYF_4$(Yb, Tm) NPs in Figure 2c clearly showed a core/shell structure, in which the Yb- and Tm-codoped $NaYF_4$ shells appeared brighter than the Fe_3O_4 cores. The core−shell structure of Fe_3O_4@$NaYF_4$ NPs was also investigated by bright field HRTEM. For instance, the HRTEM image of $Co_{0.16}Fe_{2.84}O_4$@$NaYF_4$(Yb, Er) NPs in Figure 2d showed a distinct contrast difference between the Co-doped Fe_3O_4 core and the Yb/Er codoped $NaYF_4$ shell, while the electron diffraction pattern indicated the crystalline nature of the core. Despite the presence of heavy atoms Yb and Er, the shell appeared brighter on bright field TEM image, since the contrast is determined by the thickness and crystallinity of the specimen, as well as its elemental composition. The atomic lattice fringes of 2.97 and 4.14 Å were associated with (022) and (200) planes, respectively, of the cubic Fe_3O_4 phase. The doping of Co into the Fe_3O_4 lattice, and of Yb and Er into $NaYF_4$ lattice, was confirmed by energy dispersive X-ray spectroscopy (EDX) (Figure S2). Compositional studies on Co/Yb/Er doped NPs were also carried out by X-ray photoelectron spectroscopy (XPS) and inductively coupled plasma mass spectrometry (ICP-MS) (Figure S3, Tables S3 and S4). ICP-MS results indicated a formulation of $Co_{0.16}Fe_{2.84}O_4$ for the core, and the unexpected low Co to Fe ratio was probably due to an incomplete decomposition of $Co(acac)_2$. The molar ratio of Y:Yb:Er was measured by ICP-MS as 79.3:18.6:2.1, consistent with the ratio of starting materials (Y_2O_3, Yb_2O_3, and Er_2O_3). By comparing the relative content of Fe, Co, Y, Yb, and Er obtained by ICP-MS and XPS (Table S3), it was clear that dramatically less Fe and Co was detected by the surface technique XPS, than by ICP-MS or EDX. This is consistent with the proposed core−shell structure observed by TEM.

The $Co_{0.16}Fe_{2.84}O_4$@$NaYF_4$(Yb, Er) and Fe_3O_4@$NaYF_4$(Yb, Tm) core−shell NPs described above, which are inevitably covered with oleylamine, were converted to a water-soluble form by ligand exchange with bisphosphonate polyethylene glycol conjugates (BP-PEG), as shown in Scheme S1 and Figure S4. The appearance of characteristic peaks associated with the PEG chain at 1109, 958, and 837 cm^{-1} on the IR spectrum of PEGylated NPs (Figure S5), diffraction peaks at 19° and 23° in the XRD pattern (Figure S1),[33,34] and a mass loss of up to 52.7% starting from over 200 °C on thermogravimetric curves (Figure S6) confirmed the attachment of BP-PEG.

Dynamic light scattering (DLS) experiments demonstrated that the NPs were highly dispersed in water after surface modification with BP-PEG, showing a hydrodynamic diameter (D_h) of 44 nm for $Co_{0.16}Fe_{2.84}O_4$@$NaYF_4$(Yb, Er) NPs over a concentration range from 0.01 to 1 mg/mL. Suspensions of PEGylated NPs were extremely stable and could not be precipitated by centrifugation at 10 000 rpm for 30 min. No aggregation was observed during a period of 14 h by DLS. This extreme long-term stability is presumed to be due to the strong coordinative interactions between the bisphosphonate groups and metallic sites on the surface of NPs, in keeping with earlier observations.[8,21]

Radiolabeling of NPs. The $NaYF_4$ shell of NPs was chosen in part due to a high affinity for [^{18}F]-fluoride, as fluoride binding to $NaYF_4$ has been reported previously.[27,28] Indeed, the ^{18}F-labeling efficiency of $Co_{0.16}Fe_{2.84}O_4$@$NaYF_4$(Yb, Er)-BP-PEG NPs (0.1 mg) was up to 38.5% after a brief (5 min) incubation with aqueous no-carrier-added [^{18}F]-fluoride at room temperature (Table S5). These observations were consistent with the core/shell structure of the NPs since neither $Co_{0.16}Fe_{2.84}O_4$ nor Fe_3O_4 alone showed significant binding to [^{18}F]-fluoride.[35] The labeling efficiency (% of radionuclide bound) was found to increase with the amount of NPs, which is consistent with previous observations.[35] The serum stability of $Co_{0.16}Fe_{2.84}O_4$@$NaYF_4$(Yb, Er)-BP-PEG NPs prelabeled with [^{18}F]-fluoride was determined by incubating the fluorinated particles in human serum for intervals of up to 2 h and measuring the fraction of activity remaining bound to NPs with a gamma counter after separating NPs from the supernatant by centrifugation in a NanoSep device with a cutoff size of 10K (Figure S7). Over 85% of the ^{18}F remained bound to the NPs after incubation in serum up to 2 h, slightly less than ca. 90% reported in PBS (phosphate buffered saline).[28] The initial partial release of ^{18}F from NPs into serum seemed to be a rapid process since no further changes was observed after 15 min.

Because of the previously observed strong interactions between phosphonate groups and $NaYF_4$ NPs[32] and iron oxide NPs,[33] it was expected that the NPs would have a high affinity for radiometal chelate−bisphosphonate conjugates.[8,20,21,33] Both $Co_{0.16}Fe_{2.84}O_4$@$NaYF_4$(Yb, Er)-BP-PEG and Fe_3O_4@$NaYF_4$(Yb, Tm)-BP-PEG particles showed a high affinity to ^{99m}Tc-DPA-ale (data not shown) and ^{64}Cu-$(DTCBP)_2$, which has two uncoordinated bisphosphonate groups,[8,20] with up to 96% labeling efficiency (Table S5). The ability to bind readily with [^{18}F]-fluoride and bisphosphonate conjugates of ^{64}Cu and ^{99m}Tc offers potential applications in PET and SPECT imaging.

Magnetic Resonance Properties. The r_1 and r_2 relaxivities were measured in aqueous solution at magnetic fields of 3 T and 7 T, to determine the feasibility of using these core/shell structures as MRI contrast agents. The values of relaxivities r_1 and r_2 of $Co_{0.16}Fe_{2.84}O_4$@$NaYF_4$(Yb, Er)-BP-PEG in aqueous solution at 3 T were calculated as 5 and 102 mM^{-1} s^{-1}, respectively (Figure 3a). At a higher magnetic field (7 T), r_1 and r_2 were found to be 2 and 159 mM^{-1} s^{-1}, respectively. Fe_3O_4@$NaYF_4$(Yb, Tm)-BP-PEG NPs showed a r_2 relaxivity of up to 326 mM^{-1} s^{-1}, and a r_1 value of 3 mM^{-1} s^{-1} at 3 T (Figure S8). A high r_2 value and r_2/r_1 ratio for both $Co_{0.16}Fe_{2.84}O_4$@$NaYF_4$(Yb, Er)-BP-PEG and Fe_3O_4@$NaYF_4$(Yb, Tm)-BP-PEG demonstrated their excellent potential as T_2 or T_2* contrast agents in MRI. Indeed, Fe_3O_4@$NaYF_4$(Yb, Tm)-BP-PEG NPs, as a multimodal contrast, provided a higher r_2 relaxivity (326 mM^{-1} s^{-1}) than clinically used Feridex ($r_2 \approx 107$ mM^{-1} s^{-1}, $r_2/r_1 \approx 4.65$)[36] and most iron oxide or iron nanoparticle-based single-modality T_2 MRI contrast agents reported so far.[37−39]

Optical Properties. $NaYF_4$ and its paramagnetic analogue $NaGdF_4$ have been intensively investigated as host materials, into which rare earth cations can be doped or codoped to achieve down-conversion or up-conversion fluorescence.[16,23,40,41] In order to incorporate this type of optical activity into our multimodality contrast NPs, lanthanide cations

DOI: 10.1021/acs.bioconjchem.5b00338
Bioconjugate Chem. 2016, 27, 319−328

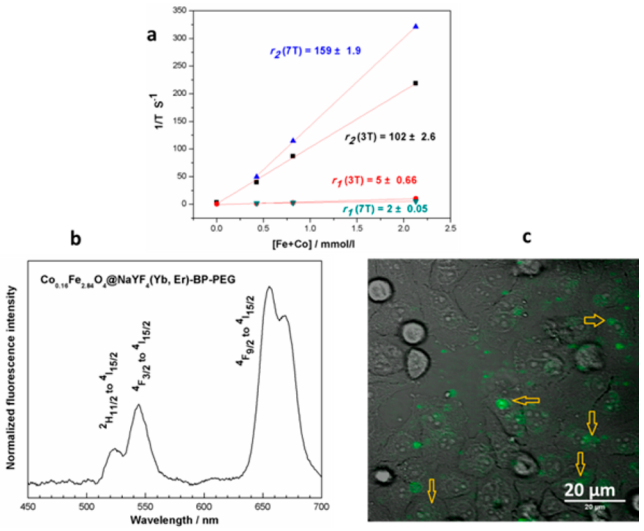

Figure 3. (a) Curve of relaxivity against the concentration of Fe+Co for $Co_{0.16}Fe_{2.84}O_4$@$NaYF_4$(Yb, Er)-BP-PEG at 3T and 7T) (concentration of Fe and Co determined by ICP-MS); (b) up-conversion spectrum of $Co_{0.16}Fe_{2.84}O_4$@$NaYF_4$(Yb, Er)-BP-PEG under excitation by a 980 nm laser; (c) transmitted infrared image of HeLa cell culture in monolayer (gray scale) incubated with $Co_{0.16}Fe_{2.84}O_4$@ $NaYF_4$(Yb, Er)-BP-PEG and fluorescence emission image (green, 490−560 nm) overlaid. Excitation wavelength 980 nm. Arrows show green fluorescence from cell-incorporated particles.

Er or Tm (active cations) were codoped with Yb^{3+} (sensitizer) into the $NaYF_4$ layer. Up-conversion fluorescent emission was then observed under excitation with a 980 nm laser. Two emission features for Fe_3O_4@$NaYF_4$(Yb, Tm)-BP-PEG at 700 and 800 nm were observed and assigned to the transitions $^3F_3$ to $^3H_6$ and $^3H_4$ to $^3H_6$ of Tm^{3+} (Figure S9), while three emission features of $Co_{0.16}Fe_{2.84}O_4$@$NaYF_4$(Yb, Er)-BP-PEG at 525, 550, and 650 nm, were assigned to the transitions from $^2H_{11/2}$ to $^4I_{15/2}$, $^4F_{3/2}$ to $^4I_{15/2}$, and $^4F_{9/2}$ to $^4I_{15/2}$ of Er^{3+} (Figure 3b). To explore the application in fluorescent imaging, $Co_{0.16}Fe_{2.84}O_4$@$NaYF_4$(Yb, Er)-BP-PEG NPs was incubated in vitro with a cultured monolayer of HeLa cancer cells in physiological saline for 24 h. Green fluorescent signals from NPs associated with cytoplasm of living HeLa cells were observed (Figure 3c), and the defined structure and position of the green fluorescence consistently identified cellular uptake of the NPs. We did not observe any fluorescent signal in the same dynamic range when a control cell culture was imaged without NP incubation. Under the high speed raster scan imaging mode, no random movement was observed and all NPs stay at the same position, indicating that NPs were incorporated inside the cells.

In Vivo Studies. To investigate the biodistribution in vivo of these NPs after systemic (intravenous) administration, solutions of the ^{18}F-radiolabeled $Co_{0.16}Fe_{2.84}O_4$@$NaYF_4$(Yb, Er)-BP-PEG (10K) (130 µL, 5.6 MBq, 40 µg Fe) and Fe_3O_4@ $NaYF_4$(Yb, Tm)-BP-PEG (2K) NPs (150 µL, 3.7 MBq, 45 µg Fe, Tables S1 and S2) were injected into the tail veins of two different mice, immediately followed by imaging by coregistered PET-MRI on a preclinical nanoScan PET•MRI scanner with 1 T magnetic field (Mediso Ltd., H-1047, Budapest, Hungary). In both cases, radioactivity was taken up by the spleen and liver within 45 min, and accumulated to a small extent in the bladder after 60 min (Figures 4a−d and S10 and S11). This biodistribution pattern for radioactivity was matched

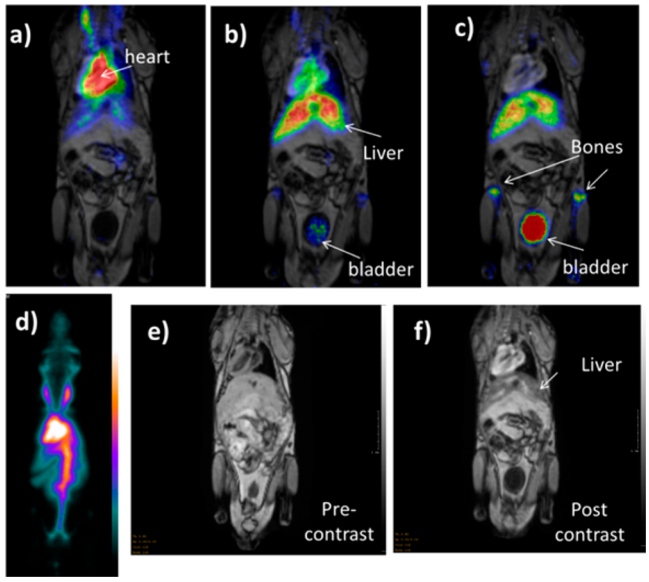

Figure 4. PET/MR images showing the dynamic biodistribution of ^{18}F radiolabeled NPs. MR images were taken immediately after PET scans, 2 h post the injection of NPs, and they were fused with PET images taken at three different time intervals (0−15 min, 45−60 min, and 105−120 min). (a) PET/MR fused image at 0−15 min, showing radioactivity mainly confined to blood pool with minor uptake in liver; (b) PET/MRI fused image at 45−60 min showing increased accumulation in liver and minor uptake in skeleton; and (c) PET/MR fused image at 105−120 min showing increased uptake in skeleton and bladder; (d) whole body PET image showing uptake of radiolabeled negatively charged NPs $Co_{0.16}Fe_{2.84}O_4$@$NaYF_4$(Yb, Er)-BP-PEG (10K) (maximum intensity projection, 30−45 min), showing radioactivity mainly confined to blood pool, with little activity in bone or bladder; (e) MR image of the mouse prior to the injection of $Co_{0.16}Fe_{2.84}O_4$@$NaYF_4$(Yb, Er)-BP-PEG (10K) NPs; (f) MR image of the mouse 2 h post injection of $Co_{0.16}Fe_{2.84}O_4$@$NaYF_4$(Yb, Er)-BP-PEG (10K) NPs. The series of images (a) to (d) shows predominantly blood pool retention of the labeled NPs at early stages post injection, giving way to liver uptake and then bone and bladder, consistent with release of radioactivity from nanoparticles in liver as free fluoride.

by darkening contrast observed on MR images (Figure 4e,f). Very little radionuclide accumulation in the skeleton (characteristic of free [^{18}F]-fluoride) was observed, indicating that the NP-radiolabel bond was reasonably stable in vivo over a 1 h time period. The later increase in radioactivity in the bladder and bone, which coincided with a decrease of radioactivity in the liver, suggests that the particles may be degraded in the liver with release of free fluoride.

In vivo PET/MRI imaging of the lymph node (LN) system was carried out using a preclinical nanoScan integrated PET/MRI system (Mediso, Budapest, Hungary) with 1 T magnet, utilizing ^{18}F-labeled $Co_{0.16}Fe_{2.84}O_4$@$NaYF_4$(Yb, Er)-BP-PEG (10 K) or Fe_3O_4@$NaYF_4$(Yb, Tm)-BP-PEG (2 K) NPs as probe. After injection of 20 µL of a solution of these NPs containing 6.3 MBq radioactivity and 20 µg Fe into the rear right foot pad of a mouse (C57BL/6, female, 6−7 weeks old, 20 g), coregistered PET and MRI images were recorded 6 h post injection. The LNs were clearly visible on PET images (Figure 5). The most prominent signal was from the popliteal LN, which is the nearest draining LN from the injection point, and the next most prominent signal was from the medial iliac LN (Figure 5b). Both LNs were evident on the MR image with a decrease in MR T_2 signal intensity compared to the

DOI: 10.1021/acs.bioconjchem.5b00338
Bioconjugate Chem. 2016, 27, 319−328

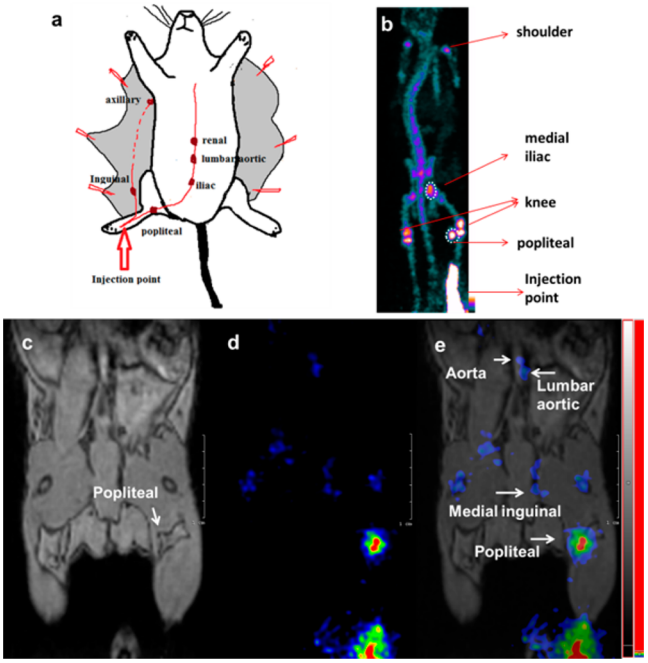

Figure 5. PET/MRI images of a normal young C57BL/6 mouse showing LNs with dual contrast provided by ^{18}F-labeled $Co_{0.16}Fe_{2.84}O_4$@$NaYF_4$(Yb, Er)-BP-PEG: (a) schematic diagram showing the connections between lymph nodes and the injection point (mouse in supine position); (b) whole body PET image showing uptake of radiolabeled NPs 7 h post injection (maximum intensity projection, mice in prone position); (c) MR image with darkening contrast at popliteal LN (coronal section); (d) PET image showing radioactivity at popliteal, inguinal, lumbar aortic, and aorta LN area (coronal section); and (e) PET/MRI fused image showing popliteal, inguinal, lumbar aortic, and aorta LN (coronal section). Some bone uptake of radioactivity is observed in (b), (d), and (e) due to gradual release of fluoride from the particles due to the long delay (7 h post injection of ^{18}F radiolabeled NPs) between injection and imaging.

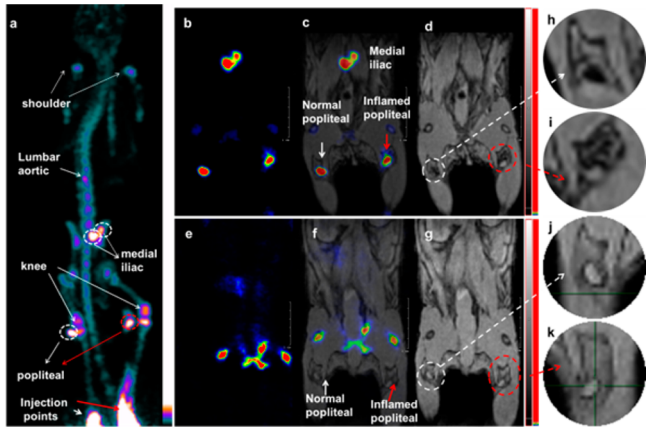

Figure 6. Lymph node PET/MRI imaging of a mouse with inflamed right leg using ^{18}F-labeled Fe_3O_4@$NaYF_4$(Yb, Tm)-BP-PEG NPs (a–d) or with [^{18}F]-fluoride only (e–g): (a) whole body PET image showing uptake of radiolabeled NPs (maximum intensity projection; bone uptake was observed due to gradual release of fluoride from NPs due to the 7 h delay post injection of NPs); (b) PET image showing popliteal and iliac lymph nodes (coronal section); (c) PET/MRI fused image (coronal section); (d) MR image (coronal section) with darkening contrast inside popliteal lymph node at left-rear (white circle) and "outside" lymph node at the inflamed right-rear (red circle) induced by injection of 30 μL 0.67 mg/mL lipopolysschrade (LPS) 18 h prior to imaging, and at iliac lymph node; (e) PET image following injection of [^{18}F]-fluoride showing no contrast in lymph nodes in the absence of NPs and prominent uptake by skeleton; (f) PET/MRI fused image following injection of [^{18}F]-fluoride, showing no radioactivity associated with lymph nodes; (g) MR image showing no difference between normal popliteal lymph node at left-rear leg (white circle) and the inflamed lymph node at right-rear leg induced by injection of 30 μL 0.67 mg/mL LPS 18 h prior to imaging; and (h–k) enlarged MR images of corresponding lymph nodes.

contralateral (control) LNs (Figure S12). Interestingly, a PET signal was also detected at the more distant lumbar aortic LN (Figure 5d and e). However, no contrast was observed at this area on MR image post injection, due to the relatively poor sensitivity of MRI (Figures 5c and S12). Because of the long delay post injection (6 h) skeletal uptake of radioactivity was also observed in the PET image consistent with gradual release of fluoride from the NPs in vivo.

To further explore the potential value of this class of NPs, a more detailed lymph node study by PET/MRI imaging was undertaken, investigating the popliteal LN in response to an acute inflammatory stimulus in the foot. A solution of ^{18}F labeled Fe_3O_4@$NaYF_4$(Yb, Tm)-BP-PEG (20 μL, 4.5 MBq, 20 μg Fe) was injected into each of the two rear footpads of a female C57BL/6 mouse in which only the right leg was inflamed. Again, uptake of particles in both popliteal and iliac LNs was identified by PET and MRI (Figures 6, S13) 6 h post injection. Interestingly, the right popliteal LN appeared on the MR image as a white spot with a darkened background while the left counterpart displayed a black spot with a white background typical of a healthy lymph node (Figure 6h and i). A possible biological rationale for this behavior is that the LPS induced a macrophage response that may have taken up sufficient numbers of the nanoparticles to be detectable by MRI. As macrophages migrating to draining lymph nodes do not enter the lymph node, but rather stay in the capsular layer, this would lead to the observed signal distribution.[42,43] Thus, while PET has the sensitivity to easily locate the relevant lymph node, MRI provided the resolution lacking in PET to delineate disease-related and hence potentially diagnostic changes in the fine structure and distribution of contrast agents in and around the LN. A control experiment was carried out with [^{18}F]-fluoride but without NPs, under the same conditions. The PET image in this case did not show any signal at the lymph nodes and only the skeleton was seen (Figure 6e and f), confirming that the PET signal in the LN of the NP-treated mice came from [^{18}F]-labeled NPs. MRI scanning without injection of the labeled NPs showed no contrast difference between the normal LN and the inflamed one.

DISCUSSION

We have presented a novel type of inorganic core–shell NP with built-in magnetic, fluorescent, and radiolabeling properties, which show potential as probes for MRI, optical imaging, and PET/SPECT imaging. Stealth features to evade the immune system and prevent opsonization are required in some imaging and therapy applications to reduce the off-target localization and toxicity of NPs, prolong their circulation time in the blood pool (where this is desirable) and deliver them to specific sites. PEGylation, using the novel bisphosphonate derivative to anchor the PEG to the NP surface, was employed not only to stabilize the particles against aggregation in solution by the steric effect, but also to modify their circulation time. PEGylated ligands with different polymeric chain lengths

DOI: 10.1021/acs.bioconjchem.5b00338
Bioconjugate Chem. 2016, 27, 319–328

were introduced on the surface of $Co_{0.16}Fe_{2.84}O_4$@$NaYF_4$(Yb, Er) and Fe_3O_4@$NaYF_4$(Yb, Tm) NPs, to produce water-soluble versions: $Co_{0.16}Fe_{2.84}O_4$@$NaYF_4$(Yb, Er)-BP-PEG and Fe_3O_4@$NaYF_4$(Yb, Tm)-BP-PEG. In both cases, PEGylation, small hydrodynamic size (≪100 nm) and low zeta-potential[44] offer the opportunity to control circulation time and avoid immediate reticulendothelial clearance where this is desired for specific applications. Indeed, the longer-chain PEGylation of $Co_{0.16}Fe_{2.84}O_4$@$NaYF_4$(Yb, Er) (10 K) (M_w = 10 kDa, $n \approx$ 227) resulted in a slightly negative zeta potential (−10 mV) and delayed clearance compared to Fe_3O_4@$NaYF_4$(Yb, Tm)-BP-PEG (2 K) (M_w = 2 kDa, $n \approx$ 45, and zeta potential of +10 mV)) (Figures 4, S10 and S11), although surface density of PEG(10K) is less than that of PEG(5K) (37.6% vs 52.7%). This suggests that the length of the PEG chain and zeta potential of NPs play important roles in biodistribution. The circulation time of $Co_{0.16}Fe_{2.84}O_4$@$NaYF_4$(Yb, Er) (10 K) is shorter than that reported previously for PEGylated iron oxide.[30] This may be attributable to reduced PEG surface coverage (36.7% vs 61%, Figure S6). The extent of PEGylation and the chain length may therefore be optimized for specific applications. Particle size combined with surface properties also plays an important role in enhancing lymphatic transport.[45,46] Small particles (less than 100 nm) are transported and taken up more readily, whereas the larger NPs are likely to remain in the injection site. PEGylation can improve the uptake in lymph nodes by reducing the nonspecific interaction between particles and proteins of the interstitium.

Convenient incorporation of readily available imaging radioisotopes such as [^{18}F]-fluoride is important for applications in radionuclide imaging. Because of the short half-life and the need for GMP conditions in the daily production of radiopharmaceuticals at hospital sites, radiolabeling procedures must be as simple as possible and avoid the requirement of costly specialist facilities. Inorganic nanoparticulate materials have previously been reported that bind [^{18}F]-fluoride rapidly with high efficiency under mild conditions.[35] The $NaYF_4$ shell of the core−shell system can efficiently carry ^{18}F as well as other radionuclides such as ^{99m}Tc or ^{64}Cu BP conjugates, and the radiolabeling of these particles is extremely simple, quick, and efficient. Release of fluoride from the NPs, allowing uptake in bone, is relatively slow compared to both lymphatic transport and reticulendothelial clearance, allowing imaging of both processes (Figures 4−6, S10 and S13).

The fluorescent properties of the codoped $NaYF_4$ shell allowed microscopic fluorescence imaging at the cellular level (Figure 3d), and could be explored as a potential visual guide during surgery.[47] NPs with stronger fluorescent emissions can be developed by deposition of additional pure or doped $NaYF_4$ layer on the core−shell structures[22] to suppress the energy transfer to surface quenchers (impurities, ligands, and solvent molecules) and to modify local crystal structure surrounding the doping cations. The balance between the thickness of the fluorescent and radiolabeled shell of $NaYF_4$ and the size and composition of the magnetic core could be adjusted to optimize the optical and magnetic properties, respectively, for applications as multimodal imaging agents.[48] For example, NPs Fe_3O_4@$NaYF_4$(Yb, Tm)-BP-PEG showed a much higher r_2 relaxivity than NPs $Co_{0.16}Fe_{2.84}O_4$@$NaYF_4$(Yb, Er)-BP-PEG (326 mM^{-1} S^{-1} vs 102 mM^{-1} S^{-1}), though both of them share a similar particle size and core-to-shell ratio (Figure S9).

Accurate location and identification of lymph nodes and detection of the pathology within them is important for studies of tumor metastasis in humans, including the identification of sentinel lymph nodes during surgery, and in rodent models for the study of immune responses to foreign antigens, transplants, and tumors. The in vivo imaging studies reported here, although not matched to a current typical clinical imaging protocol, are relevant to sentinel node imaging in support of cancer surgery and suggest several ways in which combined coregistered MR and PET imaging with a single contrast agent can provide additional information and increased confidence in image interpretation. The PET images, by virtue of lower content of irrelevant detail, allow easy identification of regions for closer examination by MRI. In addition, the greater sensitivity of PET allows detection of relevant lymph nodes distant from the disease site (e.g., Figure 5c−e) which is unlikely to be detected by MRI alone (Figure 6). The accurate presurgical location of iliac and popliteal LNs in context of the anatomy of the mouse was achieved only when the PET and MRI images were coregistered and overlaid. The improved soft tissue contrast offered by MRI compared to CT, which is conventionally combined with PET and SPECT, should offer improved presurgical mapping of lymph node locations. Moreover, the additional anatomical and functional detail in soft tissues permitted by contrast MRI (e.g., the differences in structure and contrast agent distribution in and around the lymph node between left and right popliteal nodes) in regions initially identified by PET, but which the limited resolution of PET cannot show, have the potential to provide useful diagnostic information beyond simply identifying presurgically the location of the sentinel node. This is likely to provide synergistic value when used during imaging with the new generation of clinical combined PET/MR scanners now appearing in hospitals. The fluorescence should enable further visual observation of these anatomical and functional changes during surgery and subsequently during pathological examination of excised tissues. Data from each of these imaging modalities can be combined, with reassurance that the signal comes from the same contrast agent, and hence the same biodistribution, in each modality.

CONCLUSIONS

In summary, we have reported the synthesis and characterization of the first series of $Co_xFe_{3-x}O_4$@$NaYF_4$ core−shell based NPs in which the shell was codoped with lanthanide cations providing optical imaging capabilities, and could also be radiolabeled with [^{18}F]-fluoride and radiometal−bisphosphonate conjugates, while the iron oxide-based core provided MR contrast. We have shown for the first time that the $NaYF_4$ shell can be stably modified with bisphosphonate-derived PEG and radionuclide conjugates. The particles offer trimodal imaging using PET/SPECT, MRI, and up-conversion fluorescent imaging. The NPs showed excellent colloidal stability in water and a narrow size distribution after surface modification with BP-PEG. The simple and quick radiolabeling process is a major advantage for use of these materials as PET/SPECT tracers and is essential for routine clinical use. Our in vivo studies in lymph nodes demonstrated the potential advantages of combining imaging modalities using NPs as multimodal (PET, MRI, and optical) imaging agents. In addition, these NPs could also potentially act as visual guides during surgery due to their up-conversion fluorescent properties.

DOI: 10.1021/acs.bioconjchem.5b00338
Bioconjugate Chem. 2016, 27, 319−328

EXPERIMENTAL SECTION

Materials and General Characterization. Chemicals were obtained from commercial sources and used as purchased without further purification unless otherwise specified. Human serum was obtained by filtering human male AB plasma from Sigma-Aldrich with Millex IC 0.22 μm (13 mm) hydrophilic PTFE filters. Water was obtained from an ELGA PureLab OptionQ system. Organic solvents oleylamine (90%, technical grade) and 1-octadecene (90%, technical grade) came from Fisher Scientific Ltd. Rare earth trifluoroacetate salts were prepared in house from corresponding rare earth oxides purchased from Sigma-Aldrich. Typically, the mixed powder of Y_2O_3, Yb_2O_3, and Er_2O_3 (molar ratio Y:Yb:Er = 78:20:2) was dissolved in trifluoroacetic acid at 60 °C, and water was removed by rotary evaporator to obtain light pink or white $M(CF_3COO)_3$ powder. ^{18}F and ^{64}Cu were produced using the PET Imaging Centre cyclotron at St Thomas's Hospital, London, UK. ^{99m}Tc-MDP was obtained from the Nuclear Medicine Department, Guy's and St Thomas' Foundation Trust. Thermogravimetric analysis (TGA) was performed under a flow of nitrogen (20 mL/min) with a heating rate of 5 °C/min using a TA SDT-600 thermogravimetric analyzer. XRD were recorded at room temperature on a PANalytical X'Pert PRO diffractometer using Cu Kα_1 radiation (λ = 1.540598 Å) at 40 kV, 40 mA, at a scan speed of 0.02°/s and a step size of 0.026° in 2θ. XPS spectra were recorded using a Kratos AXIS ULTRA with monochromated Al K radiation (10 kV anode potential, 15 A emission current) in fixed analyzer transmission mode (80 eV pass energy). TEM images were taken on Tecnai FEI T20 at Centre for Ultrastructural Imaging, King's College London, and HRTEM on JEOL 2100 at Nottingham Nanotechnology and Nanoscience Centre, Nottingham University, and on T20 at LEMAS, Leeds University. IR spectra were recorded on a PerkinElmer spectrum 100. DLS experiments were carried out on Zetasizer Nano ZS from Malvern Instruments with a measured angle 175° and a 632.8 nm laser. Zeta potential for all samples was measured in neutral aqueous solution with a pH value ≈ 7. Up-conversion spectra were obtained at Queen Mary University of London, using a 980 nm continuous wave diode laser modulated at a frequency of 13 Hz. The photoluminescence was dispersed in a Triax 550 spectrometer and detected with a Hamamatsu R5509−72 photomultiplier.

Synthesis of $Co_{0.16}Fe_{2.84}O_4$@$NaYF_4$(Yb, Er) NPs. First, $Co(acac)_2$ (514 mg, 2 mmol) was dissolved in a solvent mixture of 5 mL oleylamine and 15 mL 1-octadecene at 120 °C under vacuum. Under N_2 atmosphere, $Fe(CO)_5$ (4.5 mmol, 0.6 mL) was injected into the solution of $Co(acac)_2$, and then the resultant solution was heated up to 250 °C within 15 min under stirring. After being kept at 250 °C for 1 h, a solution obtained by dissolving CF_3COONa (800 mg, 5.9 mmol) and $M(CF_3COO)_3$ (M = Y, Yb, or Er; Y:Yb:Er = 78:20:2; 1000 mg; 2 mmol) in 10 mL oleyl amine and 10 mL 1-octadecene at 120 °C under vacuum, was added into the resultant black slurry under N_2 by syringe. The mixture was heated to 340 °C with a heating rate 10 °C/min. After being kept at 340 °C for 15 min, the mixture was cooled down to room temperature by removing the heating bath. The product was precipitated out by adding 30 mL ethanol and then collected by a magnet. The particles were redispersed in hexane and precipitated with ethanol twice more. Fe_3O_4@$NaYF_4$(Yb, Tm) NPs was obtained use a similar approach as $Co_{0.16}Fe_{2.84}O_4$@$NaYF_4$(Yb, Er) NPs.

Synthesis of Fe_3O_4@$NaYF_4$(Yb, Tm) NPs. First, CF_3COONa (800 mg, 5.9 mmol) and $M(CF_3COO)_3$ (M = Y, Yb, or Tm; Y:Yb:Tm = 75:20:5; 1000 mg; 2 mmol) were dissolved in 10 mL oleyl amine and 10 mL 1-octadecene at 120 °C under vacuum for at least 30 min. Under N_2 atmosphere, $Fe(CO)_5$ (7 mmol, 0.9 mL) was injected into the solution, and then the resultant solution was heated up to 200 °C within 15 min under stirring. The mixture was maintained at 200 °C for 20 min under N_2, and then heated to 340 °C with a heating rate 10 °C/min. After being kept at 340 °C for 1 h, the mixture was cooled down to room temperature by removing the heating bath. The product was precipitated out by adding 30 mL ethanol and then collected by a magnet. The particles were redispersed in hexane and precipitated with ethanol twice more.

PEGylation of NPs. BP-PEG prepared as described elsewhere[8] (10 kDa, 20 mg) was dissolved in a mixture of methanol (16 mL) and ethanol (4 mL), and then 3 mL of a hexane suspension containing ca. 60 mg synthesized $Co_{0.16}Fe_{2.84}O_4$@$NaYF_4$(Yb, Er) NPs was added under sonication using a standard laboratory sonic bath. The resultant brown solution was treated with excess hexane to precipitate out NPs. To remove uncoordinated ligands, the product was redispersed in ethanol and precipitated out by adding hexane. The same procedure was carried out to conjugate BP-PEG (2 kDa) with Fe_3O_4@$NaYF_4$(Yb, Tm) NPs.

Radiolabeling of NPs with [^{18}F]-Fluoride, ^{99m}Tc-DPA-ale, or ^{64}Cu-(DTCBP)$_2$. Typically, 100 μL of [^{18}F]-fluoride in ^{18}O-water direct from target was added into a Nanosep centrifugal device with omega membrane (from Sigma-Aldrich, molecular weight cutoff size = 30 000) containing 400 μL NP suspension. After incubation at room temperature for 5−15 min, the suspension was centrifuged at 10 000 rpm (Eppendorf centrifuge 5424) for 10 min to separate the NPs from solution. The radioactivity remaining in filtrate and on NPs was measured by a gamma counter or a CRC-25R dose calibrator (Capintec, USA). Labeling efficiency was calculated by dividing the radioactivity on NPs by the sum of that in supernatant and on NPs. Triplicate measurements were carried out at each concentration of NPs. Radiolabeling with ^{99m}Tc-DPA-ale or ^{64}Cu bis(dithiocarmabate) bisphosphonate conjugate (^{64}Cu-(DTCBP)$_2$) was carried out via the previously published procedures.[8,21]

Stability of [^{18}F]-Fluoride Labeled NPs in Human Serum. ^{18}F-Fluoride labeled radiolabeled NPs were dissolved in 500 μL serum and left at 37 °C for different periods of time. Then NPs were separated by Nanosep centrifugation at 14 000 rpm (Eppendorf centrifuge 5424) for at least 15 min. The radioactivity in serum and on NPs was measured by gamma counter, respectively. Triplicate samples were measured at each time point.

T_1, T_2, and T_2* Relaxivity Measuremen. MR imaging was performed with a standard extremity flex coil on a clinical 3T Philips Achieva MRI scanner (Philips Healthcare, Best, The Netherlands). T_1 mapping was obtained by using a 2D sequence that employs two nonselective inversion pulses with inversion times ranging from 20 to 2000 ms, followed by eight segmented readouts for eight individual images.[49] The two imaging trains result in a set of 16 images per slice with increasing inversion times (FOV = 200 × 200 mm^2, matrix = 200 × 179 mm^2, in-plane resolution = 1 × 1.12 mm^2, measured slice thickness = 3 mm, slices = 16, TR/TE = 3.2/1.6 ms, FA = 10°). T_2 was determined with a 2D multispin−echo sequence (FOV = 200 × 200 mm, matrix = 200 × 200, measured slice

DOI: 10.1021/acs.bioconjchem.5b00338
Bioconjugate Chem. 2016, 27, 319−328

thickness = 3 mm, ETL = 5, TE = 10 ms, TR = 725 ms, FA = 90°). The acquired imaging data were transferred to a computer running *Matlab* and analyzed using an in-house *Matlab* tool to receive the relaxation times T_1 and T_2 for each SPIO concentration. *Excel* was used to plot the relaxation rates over the concentration and to fit a linear function to determine the relaxivity values (i.e., gradient of linear fit).

In Vivo PET/MRI Imaging. Five 6−7-week-old female C57 black mice with a weight of 20−21 g were used. Animal experiments were carried out at Nanobiotechnology & In Vivo Imaging Center of Semmelweis University, with permission from the local institutional animal ethics committee and in compliance with the relevant European Union and Hungarian regulations. Inflammation was induced by injection of 30 μL 0.67 mg/mL lipopolysaccharide (LPS) into the footpad of the right-rear leg, 18 h prior to the injection of NPs. PET/MRI images were recorded on a nanoScan integrated PET/MRI system (Mediso, Budapest, Hungary) in which the MR is a preclinical 1T MRI scanner (M2, Aspect Imaging) with horizontal bore magnet, solenoid coil (diameter of 35 mm), and 450 mT/m gradients. Mice were anaesthetized with isoflurane and placed in prone position on the MRI bed. In the case of lymph node imaging with NP $Co_{0.16}Fe_{2.84}O_4$@ $NaYF_4$(Yb, Er)-BP-PEG, after the precontrast MR scan, 20 μL NPs solution in saline containing 6.3 MBq ^{18}F-fluoride radioactivity and 40 μg Fe was injected into the footpad of the right-rear leg (Tables S1 and S2). PET scanning was started 6 h after injection. Acquisition took place in 1−5 coincidence mode with 5 ns coincidence window, 400−600 keV energy window, 94.7 mm scan range, and acquisition time was 30 min. A 3D expectation maximization (3D EM) PET reconstruction algorithm (Mediso Tera-Tomo TM) was applied to produce PET images including corrections for attenuation and scatter, dead time, decay, and randoms. After 8 iterations the reconstruction stopped, resulting in images with 0.1 mm voxel size and time frames of 8 × 15 min. MR scanning was performed immediately after PET. The images of the two modalities were fused automatically. The same procedure was carried out for intravenously injected contrast agent, but radiolabeled nanoparticles were injected via the tail vein and PET scanning started immediately after the injection with total acquisition time of 2 h instead of 30 min.

In Vitro Fluorescent Cell Imaging. A monolayer HeLa cell culture (grown in RPMI 1640 medium supplemented with 2% of fetal calf serum) was incubated for 24 h with the nanoparticle dispersion. Particles that were not attached or internalized to cells were washed by physiological saline. Cell culture was imaged in the Femto2D two-photon microscope, under an excitation laser of 980 nm. We also imaged a washed but not nanoparticle-incubated control HeLa cell monolayer in the same conditions. *Z*-stacks of 1 μm *z*-steps at 35 μm *z*-range were recorded in both cases in order to find the inner part of the cells. A few diffusing particles in the solution above the cells were clearly distinguishable from those that did not move, attached inside the cells. Transmitted infrared light and green fluorescence emission (490−560 nm) was detected in separate channels.

■ ASSOCIATED CONTENT

Supporting Information

The detailed information for in vivo imaging; synthesis scheme of NPs; XRD, EDX, XPS, ICP-MS, and IR results of NPs; structure of ligands and functionalized NPs; TGA; radiolabeling; MR relaxivities of NPs; stability of radiolabeled NPs; dynamic biodistribution of NPs; PET/MR images; and pre- and postcontrast MR images. The Supporting Information is available free of charge on the ACS Publications website at DOI: 10.1021/acs.bioconjchem.5b00338.

■ AUTHOR INFORMATION

Corresponding Authors

*E-mail: mark.a.green@kcl.ac.uk.
*E-mail: philip.blower@kcl.ac.uk.

Notes

The authors declare no competing financial interest.

■ ACKNOWLEDGMENTS

We thank Prof. Martin Schroder at School of Chemistry, Nottingham University, for the access to TGA equipment, Dr. Michael Ward at LEMAS Centre, Leeds University, for his assistance on HRTEM, Drs. Alice Warley and Gama Vizcay, at Centre for Ultra Structural Imaging, King's College London for TEM, Dr. Haitao Ye at School of Engineering and Applied Science, Aston University for XPS, Prof. Shuhong Yu and Mr. Liang Dong at School of Chemistry, University of Science and Technology of China, for up-conversion spectrum measurement. The help from László Papp, Sándor Hóbor and Gábor Németh from Mediso is kindly acknowledged. RTMR and DM would like to thank EU COST action TD1007 on PET-MRI. This research was supported by the Centre of Excellence in Medical Engineering Centre funded by the Wellcome Trust and EPSRC under grant number WT088641/Z/09/Z, and the King's College London and UCL Comprehensive Cancer Imaging Centre funded by CRUK and EPSRC in association with the MRC and DoH (England), and by the National Institute for Health Research (NIHR) Biomedical Research Centre at Guy's and St Thomas' NHS Foundation Trust and King's College London. PET and SPECT scanning equipment was funded by an equipment grant from the Wellcome Trust. IH thanks EU FP7 for Marie Curie CIG 303535. The views expressed are those of the author(s) and not necessarily those of the NHS, the NIHR or the Department of Health.

■ REFERENCES

(1) Shao, Y. P., Cherry, S. R., Farahani, K., Meadors, K., Siegel, S., Silverman, R. W., and Marsden, P. K. (1997) Simultaneous PET and MR Imaging. *Phys. Med. Biol. 42*, 1965−1970.

(2) Marsden, P. K., Strul, D., Keevil, S. F., Williams, S. C. R., and Cash, D. (2002) Simultaneous PET and NMR. *Br. J. Radiol. 75*, S53−S59.

(3) Mackewn, J. E., Strul, D., Hallett, W. A., Halsted, P., Page, R. A., Keevil, S. F., Williams, S. C. R., Cherry, S. R., and Marsden, P. K. (2004) Design and Development of an MR-Compatible PET Scanner for Imaging Small Animals. In *IEEE Nucl. Sci. Symp. Conf. Rec.* (Seibert, J. A., Ed.) pp 3271−3274, Vols *1*−7.10.1109/NSSMIC.2004.1466386

(4) Bolus, N. E., George, R., Washington, J., and Newcomer, B. R. (2009) PET/MRI: the Blended-modality Choice of the Future. *J. Nucl. Med. Technol. 37*, 63−71 quiz 72−3.

(5) Baker, M. (2010) The Whole Picture. *Nature 463*, 977−980.

(6) Jennings, L. E., and Long, N. J. (2009) 'Two Is Better Than One'-probes for Dual-modality Molecular Imaging. *Chem. Commun.*, 3511−3524.

(7) Ali, Z., Abbasi, A. Z., Zhang, F., Arosio, P., Lascialfari, A., Casula, M. F., Wenk, A., Kreyling, W., Plapper, R., Seidel, M., et al. (2011) Multifunctional Nanoparticles for Dual Imaging. *Anal. Chem. 83*, 2877−2882.

DOI: 10.1021/acs.bioconjchem.5b00338
Bioconjugate Chem. 2016, 27, 319−328

(8) Torres Martin de Rosales, R. T. M., Tavare, R., Paul, R. L., Jauregui-Osoro, M., Protti, A., Glaria, A., Varma, G., Szanda, I., and Blower, P. J. (2011) Synthesis of Cu^{64}(II)-bis-(dithiocarbamatebisphosphonate) and Its Conjugation with Superparamagnetic Iron Oxide Nanoparticles: *in vivo* Evaluation as Dual-modality PET-MRI Agent. *Angew. Chem., Int. Ed. 50*, 5509−5513.
(9) Cho, E. C., Glaus, C., Chen, J. Y., Welch, M. J., and Xia, Y. N. (2010) Inorganic Nanoparticle-based Contrast Agents for Molecular Imaging. *Trends Mol. Med. 16*, 561−573.
(10) Lee, D.-E., Koo, H., Sun, I.-C., Ryu, J. H., Kim, K., and Kwon, I. C. (2012) Multifunctional Nanoparticles for Multimodal Imaging and Theragnosis. *Chem. Soc. Rev. 41*, 2656−2672.
(11) Baker, M. (2010) Nanotechnology Imaging Probes: Smaller and More Stable. *Nat. Methods 7*, 957−962.
(12) Shen, J., Sun, L.-D., Zhang, Y.-W., and Yan, C.-H. (2010) Superparamagnetic and Upconversion Emitting Fe_3O_4/$NaYF_4$:Yb,Er Hetero-nanoparticles *via* a Crosslinker Anchoring Strategy. *Chem. Commun. 46*, 5731−5733.
(13) Hu, D., Chen, M., Gao, Y., Li, F., and Wu, L. (2011) A Facile Method to Synthesize Superparamagnetic and Up-conversion Luminescent $NaYF_4$:Yb, Er/Tm@SiO_2@Fe_3O_4 Nanocomposite Particles and Their Bioapplication. *J. Mater. Chem. 21*, 11276−11282.
(14) Gao, J. H., Gu, H. W., and Xu, B. (2009) Multifunctional Magnetic Nanoparticles: Design, Synthesis, and Biomedical Applications. *Acc. Chem. Res. 42*, 1097−1107.
(15) Zhou, J., Yu, M., Sun, Y., Zhang, X., Zhu, X., Wu, Z., Wu, D., and Li, F. (2011) Fluorine-18-labeled Gd^{3+}/Yb^{3+}/Er^{3+} Co-doped $NaYF_4$ Nanophosphors for Multimodality PET/MR/UCL Imaging. *Biomaterials 32*, 1148−1156.
(16) Ren, G. Z., Zeng, S. J., and Hao, J. H. (2011) Tunable Multicolor Upconversion Emissions and Paramagnetic Property of Monodispersed Bifunctional Lanthanide-Doped $NaGdF_4$ Nanorods. *J. Phys. Chem. C 115* (41), 20141−20147.
(17) Tian, G., Gu, Z., Zhou, L., Yin, W., Liu, X., Yan, L., Jin, S., Ren, W., Xing, G., Li, S., and Zhao, Y. (2012) Mn^{2+} Dopant-Controlled Synthesis of $NaYF_4$:Yb/Er Upconversion Nanoparticles for *in vivo* Imaging and Drug Delivery. *Adv. Mater. 24* (9), 1226−1231.
(18) Lewin, M., Carlesso, N., Tung, C. H., Tang, X. W., Cory, D., Scadden, D. T., and Weissleder, R. (2000) Tat Peptide-Derivatized Magnetic Nanoparticles Allow *in vivo* Tracking and Recovery of Progenitor Cells. *Nat. Biotechnol. 18* (4), 410−414.
(19) Wang, L., Neoh, K. G., Kang, E. T., Shuter, B., and Wang, S.-C. (2009) Superparamagnetic Hyperbranched Polyglycerol-Grafted Fe_3O_4 Nanoparticles as a Novel Magnetic Resonance Imaging Contrast Agent: an *in vitro* Assessment. *Adv. Funct. Mater. 19* (16), 2615−2622.
(20) Torres Martin de Rosales, R. T. M., Finucane, C., Mather, S. J., and Blower, P. J. (2009) Bifunctional Bisphosphonate Complexes for the Diagnosis and Therapy of Bone Metastases. *Chem. Commun.*, 4847−4849.
(21) Torres Martin de Rosales, R. T. M., Tavare, R., Glaria, A., Varma, G., Protti, A., and Blower, P. J. (2011) Tc-^{99m}-Bisphosphonate-Iron Oxide Nanoparticle Conjugates for Dual-modality Biomedical Imaging. *Bioconjugate Chem. 22* (3), 455−465.
(22) Zhong, C., Yang, P., Li, X., Li, C., Wang, D., Gai, S., and Lin, J. (2012) Monodisperse Bifunctional Fe_3O_4@$NaGdF_4$:Yb/Er@$NaGdF_4$:Yb/Er Core-shell Nanoparticles. *RSC Adv. 2* (8), 3194−3197.
(23) Xia, A., Gao, Y., Zhou, J., Li, C. Y., Yang, T. S., Wu, D. M., Wu, L. M., and Li, F. Y. (2011) Core-shell $NaYF_4$:Yb^{3+},Tm^{3+}@Fe_xO_y Nanocrystals for Dual-modality T_2-enhanced Magnetic Resonance and NIR-to-NIR Upconversion Luminescent Imaging of Small-Animal Lymphatic Node. *Biomaterials 32* (29), 7200−7208.
(24) He, H., Xie, M. Y., Ding, Y., and Yu, X. F. (2009) Synthesis of Fe_3O_4@LaF_3:Ce,Tb Nanocomposites with Bright Fluorescence and Strong Magnetism. *Appl. Surf. Sci. 255* (8), 4623−4626.
(25) Boyer, J.-C., Cuccia, L. A., and Capobianco, J. A. (2007) Synthesis of Colloidal Upconverting $NaYF_4$: Er^{3+}/Yb^{3+} and Tm^{3+}/Yb^{3+} Monodisperse Nanocrystals. *Nano Lett. 7* (3), 847−852.
(26) Ye, X., Collins, J. E., Kang, Y., Chen, J., Chen, D. T. N., Yodh, A. G., and Murray, C. B. (2010) Morphologically Controlled Synthesis of Colloidal Upconversion Nanophosphors and Their Shape-directed Self-assembly. *Proc. Natl. Acad. Sci. U. S. A. 107* (52), 22430−22435.
(27) Xiong, L., Yang, T., Yang, Y., Xu, C., and Li, F. (2010) Long-term *in vivo* Biodistribution Imaging and Toxicity of Polyacrylic Acid-coated Upconversion Nanophosphors. *Biomaterials 31* (27), 7078−7085.
(28) Sun, Y., Yu, M., Liang, S., Zhang, Y., Li, C., Mou, T., Yang, W., Zhang, X., Li, B., Huang, C., et al. (2011) Fluorine-18 Labeled Rare-earth Nanoparticles for Positron Emission Tomography (PET) Imaging of Sentinel Lymph Node. *Biomaterials 32* (11), 2999−3007.
(29) Mi, C. C., Tian, Z. H., Cao, C., Wang, Z. J., Mao, C. B., and Xu, S. K. (2011) Novel Microwave-assited Solvothermal Synthesis of NaYF4:Yb, Er Upconvertion Nanoparticles and Their Application in Cancer Cell Imaing. *Langmuir 27*, 14632−14637.
(30) Zhang, J. P., Mi, C. C., Wu, H. Y., Huang, H. Q., Mao, C. B., and Xu, S. K. (2012) Synthesis of NaYF4:Yb/Er/Gd Up-conversion Luminescent Nanoparticles and Luminescence Resonance Energy Transfer-based Protein Detection. *Anal. Biochem. 421*, 673−679.
(31) Chen, J., Guo, C. R., Wang, M., Huang, M., Wang, L., Mi, L. P., Li, C. C., Fang, J., Mao, X. X., B, C., and Xu, S. K. (2011) Controllable synthesis of NaYF4 : Yb,Er upconversion nanophosphors and their application to in vivo imaging of Caenorhabditis elegans. *J. Mater. Chem. 21*, 2632−2638.
(32) Boyer, J. C., Manseau, M. P., Murray, J. I., and van Veggel, F. (2010) Surface Modification of Upconverting $NaYF_4$ Nanoparticles with PEG-phosphate Ligands for NIR (800 nm) Biolabeling within the Biological Window. *Langmuir 26* (2), 1157−1164.
(33) Sandiford, L., Phinikaridou, A., Protti, A., Meszaros, L. K., Cui, X., Yan, Y., Frodsham, G., Williamson, P. A., Gaddum, N., Botnar, R. M., et al. (2012) Bisphosphonate-anchored PEGylation and Radiolabeling of Superparamagnetic Iron Oxide: long-circulating Nanoparticles for *in vivo* Multimodal (T_1 MRI-SPECT) Imaging. *ACS Nano 7* (1), 500−512.
(34) Wang, Q., Dong, Z., Du, Y., and Kennedy, J. F. (2007) Controlled Release of Ciprofloxacin Hydrochloride from Chitosan/polyethylene glycol Blend Films. *Carbohydr. Polym. 69* (2), 336−343.
(35) Jauregui-Osoro, M., Williamson, P. A., Glaria, A., Sunassee, K., Charoenphun, P., Green, M. A., Mullen, G. E. D., and Blower, P. J. (2011) Biocompatible Inorganic Nanoparticles for ^{18}F Fluoride Binding with Applications in PET Imaging. *Dalton Trans. 40* (23), 6226−6237.
(36) Jung, C. W., and Jacobs, P. (1995) Physical and Chemical Properties of Superparamagnetic Iron-Oxide MR Contrast Agents Ferumoxides, Ferumoxtran, Ferumoxsil. *Magn. Reson. Imaging 13* (5), 661−674.
(37) Lacroix, L.-M., Frey Huls, N., Ho, D., Sun, X., Cheng, K., and Sun, S. (2011) Stable Single-Crystalline Body Centered Cubic Fe Nanoparticles. *Nano Lett. 11* (4), 1641−1645.
(38) Poselt, E., Kloust, H., Tromsdorf, U., Janschel, M., Hahn, C., Masslo, C., and Weller, H. (2012) Relaxivity Optimization of a PEGylated Iron-Oxide-Based Negative Magnetic Resonance contrast Agent for T_2-Weighted Spin-echo Imaging. *ACS Nano 6* (2), 1619−1624.
(39) Li, Z., Yi, P. W., Sun, Q., Lei, H., Zhao, H. L., Zhu, Z. H., Smith, S. C., Lan, M. B., and Lu, G. Q. (2012) Ultrasmall Water-soluble and Biocompatible Magnetic Iron Oxide nanoparticles as Positive and Negative Dual Contrast Agents. *Adv. Funct. Mater. 22* (11), 2387−2393.
(40) Priyam, A., Idris, N. M., and Zhang, Y. (2012) Gold Nanoshell Coated $NaYF_4$ Nanoparticles for Simultaneously Enhanced Upconversion Fluorescence and Darkfield Imaging. *J. Mater. Chem. 22* (3), 960−965.
(41) Wang, L. L., Qin, W. P., Liu, Z. Y., Zhao, D., Qin, G. S., Di, W. H., and He, C. F. (2012) Improved 800 nm Emission of Tm^{3+} Sensitized by Yb^{3+} and Ho^{3+} in beta-$NaYF_4$ Nanocrystals under 980 nm Excitation. *Opt. Express 20* (7), 7602−7607.

DOI: 10.1021/acs.bioconjchem.5b00338
Bioconjugate Chem. 2016, 27, 319−328

(42) Yoo, J. S., Lee, S. C., Jow, Z. Y., Koh, P. Y. X., and Chang, Y. T. (2014) A Macrophage-Specific Fluorescent Probe for Intraoperative Lymph Node Staging. *Cancer Res. 74* (1), 44−55.
(43) Dukhin, S. S., and Labib, M. E. (2013) Convective diffusion of nanoparticles from the epithelial barrier toward regional lymph nodes. *Adv. Colloid Interface Sci. 199−200*, 23−43.
(44) Li, S. D., and Huang, L. (2008) Pharmacokinetics and Biodistribution of Nanoparticles. *Mol. Pharmaceutics 5* (4), 496−504.
(45) Reddy, S. T., Rehor, A., Schmoekel, H. G., Hubbell, J. A., and Swartz, M. A. (2006) *In vivo* Targeting of Dendritic Cells in Lymph Nodes with Poly(propylene sulfide) Nanoparticles. *J. Controlled Release 112* (1), 26−34.
(46) Bumb, A., Regino, C. S., Egen, J., Bernardo, M., Dobson, P., Germain, R., Choyke, P., and Brechbiel, M. (2011) Trafficking of a Dual-Modality Magnetic Resonance and Fluorescence Imaging Superparamagnetic Iron Oxide-Based Nanoprobe to Lymph Nodes. *Mol. Imaging Biol. 13* (6), 1163−1172.
(47) Orosco, R. K., Tsien, R. Y., and Nguyen, Q. T. (2013) Fluorescence Imaging in Surgery. *IEEE Rev. Biomed. Eng. 6*, 178−187.
(48) Vuong, Q. L., Berret, J.-F., Fresnais, J., Gossuin, Y., and Sandre, O. (2012) A Universal Scaling Law to Predict the Efficiency of Magnetic Nanoparticles as MRI T_2-Contrast Agents. *Adv. Healthcare Mater. 1* (4), 502−512.
(49) Blume, U., Orbell, J., Waltham, M., Smith, A., Razavi, R., and Schaeffter, T. (2009) 3D T_1 mapping for the Characterization of Deep Vein Thrombosis. *MAGMA 22*, 375−383.

DOI: 10.1021/acs.bioconjchem.5b00338
Bioconjugate Chem. 2016, 27, 319−328